Probing charge order and hidden topology at the atomic scale by cryogenic scanning transmission electron microscopy and spectroscopy

M.-W. Chu [1,*] G. Y. Guo [2,3] W. T. Chen [1] M. H. Lee,[1] S. H. Lee,[1] Y.-C. Lai,[1] C. H. Du [4] and C. H. Chen[1]

[1]*Center for Condensed Matter Sciences and Center of Atomic Initiative for New Materials, National Taiwan University, Taipei 106, Taiwan*
[2]*Department of Physics, National Taiwan University, Taipei 106, Taiwan*
[3]*Physics Division, National Center for Theoretical Sciences, Hsinchu 300, Taiwan*
[4]*Department of Physics, Tamkang University, Taipei 251, Taiwan*

Charge orders (COs) and entangled topology denote the fundamentals of correlated electron systems at low temperatures, and their profound revelation at atomic scale awaits experimental advances. Here, we report such a spatially resolved investigation using cryogenic atomic-scale electron microscopy and spectroscopy at 100 K, with the CO insulator of $HgMn_7O_{12}$ below 240 K as an exemplification. By the cryogenic technique, we can resolve the charge and lattice characteristics of the insulating CO phase at atomic resolution and identify the order parameters (OPs) at play as charge-density-modulated ($\sim$31.4 Å, modulation length) and antiphase ($\sim$10.5 Å) OPs. Both OPs are largely unaddressed forms of COs in correlated oxides and display the emergent topology of intertwining mesoscopic stripes of 10–40 nm in width and $\geqslant$500 nm in length, distinctly different from the atomically narrow CO stripes conventional to correlated systems and depicting the unique electronic contour of the phase. This preliminary demonstration of the cryogenic unveiling of the OPs and topological landscape paves the way to disentangling the multifarious COs and hidden topology in condensed matters and, meanwhile, calls for further developments in the atomic-scale cryogenic spectral probing at an enhanced speed.

I. INTRODUCTION

Electronic phase transitions enrich the phase diagram of correlated electron systems and are customarily entangled with charge orders (COs) thereby [1–3]. CO stripes represent a conventional form of the COs and feature atomically narrow lines of charges embedded in the crystalline matrixes with typically nonlocal Coulomb interactions [1,2]. The translation symmetry of the underlying lattices is broken by the CO stripes, and a unidirectional super-periodicity perpendicular to the one-dimensional stripes concomitantly arises [1,2].

The CO stripes are ubiquitous in hole-doped correlated insulators of copper [4–10], nickel [11–16], and manganese oxides [17–19], and the topology of the textured stripes casts an electronically modulated contour in the phases [1,2,20,21]. The renowned smectic CO in cuprates is a classical manifestation of the CO stripes and intimately intertwined with the related superconductivity [1,2,7,8,20]. Analogous CO stripes in nickelates hint on the ground-state magnetic order [13,14], and those in manganites underline the associated colossal magnetoresistance (CMR) [17–19].

With these apparent impacts of the CO stripes [1,2,7,8,13,14,17–21], direct imaging of the topological charge contour becomes increasingly important for uncovering the electronic phase in detail and demands techniques that combine microscopic and spectroscopic capabilities at atomic scale. The state-of-the-art scanning tunneling microscopy at atomic resolution provides a prime solution and is mainly suitable to metals, namely the superconducting cuprate family [9,10]. Many doped correlated oxides such as certain nickelates and manganites [11–19], however, are insulators and require another methodology yet to be explored.

Here, we report such an atomic-scale tackling of COs and incipient topology in a hole-doped insulator of quadruple-perovskite $HgMn_7O_{12}$ (HMO) [22] using cryogenic scanning transmission electron microscopy (STEM) and electron energy-loss spectroscopy (EELS) at 100 K, which represents our low-temperature (LT) limit upon maintaining atomic resolution [23]. While the atomic-scale STEM-EELS scrutiny of metallic and insulating phases at room temperature (RT) has been demonstrated [24,25], the LT development is only at its infancy [23,26–29]. The HMO with a reported CO transition at 240 K is adequate for our 100 K setup and employed as the exemplification. Notably, the cryogenic STEM-EELS reveals the emergent forms of COs in the HMO by charge-density-modulated (CDM) and antiphase (AP) order parameters (OPs). The constituent topology of mesoscopic intertwining stripes by the OPs surpasses the characteristic microscopic length scale of conventional atomically narrow CO stripes [1,2] and composes the textured electronic contour of the CO phase in HMO. The capability of cryogenic STEM-EELS in tackling the exemplified CO phenomena can shed light on problems with complex charge-lattice coupling across material disciplines [1–3]. A group-theoretical practice for the OP symmetry and conjugated topology in COs is also proposed.

---

*Corresponding author: chumingwen@ntu.edu.tw

II. EXPERIMEMTAL DETAILS

The high-pressure growth of polycrystalline HMO bulks with stoichiometric Hg and Mn has been reported [22]. The electron diffraction and dark-field (DF) transmission electron microscopy (TEM) imaging were conducted on JEOL 2000FX. The STEM high-angle annular DF (HAADF) imaging and STEM-EELS spectral probing were performed on spherical-aberration-corrected JEOL 2100FX equipped with Gatan Enfina EELS and a JEOL liquid-nitrogen stage, with the respective HAADF and STEM-EELS collection angles of 70–190 and 30 mrad [24,25]. Both electron microscopes were operated at 200 keV, and the specimens were prepared by mechanical polishing and ion milling. The cryogenic investigations were subject to a temperature limitation of 100 K and a temperature precision on the sample of ± 5 K. The thickness of the investigated polycrystalline grains is 0.6–0.7 λ (λ, inelastic mean-free path) and each polycrystalline grain (size, $\sim$tens of micrometers) represents a single-crystalline area. All STEM-HAADF images (acquisition time, $\sim$8 s) were Bragg filtered to reduce noise mainly arising from liquid-nitrogen bubbling that degrades our STEM spatial resolution from $\sim$1 Å at RT to $\sim$1.3 Å at 100 K. Each STEM-EELS dataset at RT and 100 K was optimally completed within $\sim$60 s (spectral dispersion, 0.3 eV per pixel) to mitigate the effect of concomitant specimen drift at 100 K. The RT and LT results are reproducible in altogether seven rounds of temperature-variable experiments using polycrystalline bulks from four different batches and are free from suspicious beam damages. The polycrystalline nature of the HMO renders all TEM, STEM, and EELS characterizations highly challenging.

III. RESULTS AND DISCUSSION

Figure 1(a) shows the parent HMO crystallized in cubic $Im\bar{3}$ symmetry ($a = 7.393$ Å) [22]. The nominal quadruple-perovskite $A_4B_4O_{12}$ formula of this cubic phase is of $(Hg^{+2}Mn_3^{+3})Mn_3^{+3.25}O_{12}$ due to the Mn B-site hole doping by the quarter Mn A-site substitution by Hg^{+2} [22]. In this paper, we are particularly interested in the CO phase below 240 K, with the respective symmetries above and below the 240 K transition being reported as rhombohedral $R\bar{3}$ ($a = 7.379$ Å, $\alpha = 90.379°$) and orthorhombic $Pnn2$ ($a = 7.223$ Å, $b = 7.325$ Å, and $c = 7.585$ Å) [22]. Our cryogenic STEM-EELS elaborations on the LT CO phase below 240 K commence with electron-scattering reiterations of the documented $R\bar{3}$ and $Pnn2$ symmetries [22], considering a firm determination of the crystal symmetries represents a crucial first step toward a systematic understanding of the relevant charge-lattice interplays [25]. The previously exploited x-ray powder diffraction technique for deriving the $R\bar{3}$ and $Pnn2$ symmetries is insensitive to weak structural distortions and can, therefore, lead to an average higher symmetry of a given phase [25]. The strong scattering power of electrons employed hereby is advantageous in resolving such a symmetry subtlety [25].

Figures 1(b)–1(d) show the direct probing of symmetry elements by convergent-beam electron diffraction for the HMO at RT [25]. The resolved symmetry characteristics in the corresponding whole-pattern and bright-field scattering
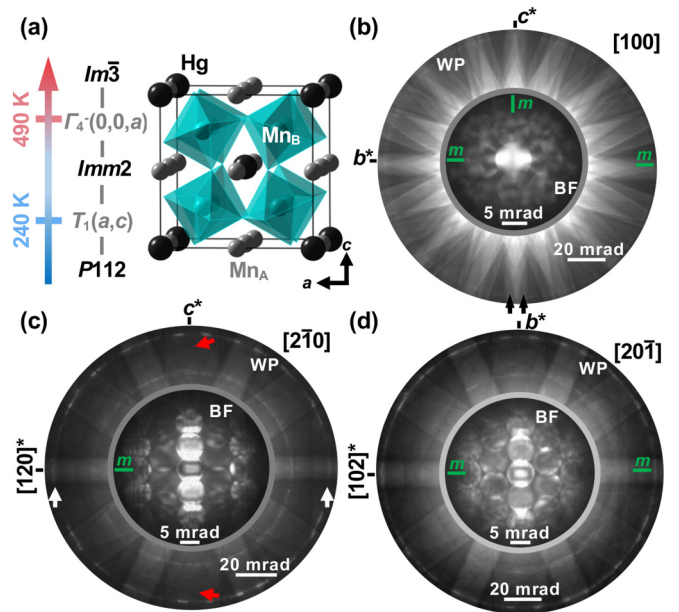

FIG. 1. (a) The cubic $HgMn_7O_{12}$ (HMO) and transition to $Imm2$ ($P112$) below 490 (240) K. The group-theoretical analysis: Γ_4^--(0,0,a) for $Imm2$ and T_1-(a, c) for $P112$. The room temperature convergent-beam electron diffraction patterns in (b) [100], (c) [2–10], and (d) [20–1] zones. Bright-field (BF) whole-pattern (WP), inner (outer) pattern. m, mirror operation. The respective BF and WP symmetries of 2mm and m in (b), m and 1 in (c), and m and m in (d) lead to the mm2 point group and, in conjunction with the reflection conditions by selected-area electron diffraction [31], identify the space group of $Imm2$. Pairs of black, white, and red arrows in WPs guides for the eyes for capturing the missing mirror operations with respect to origin.

in Figs. 1(b)–1(d) revise the RT symmetry as orthorhombic $Imm2$ ($c \sim 1.025a$, $a \approx b$) [25,30,31], instead of $R\bar{3}$. At 100 K, thorough examinations of the reflection conditions within the selected-area electron diffraction patterns in Figs. 2(a)–2(e) revise the LT monoclinic symmetry as $P112$, with the nonorthogonal angle of γ and the lattice parameters otherwise like the $Pnn2$ [22]. Figures 2(d) and 2(e) further unveil unidirectional superlattices along the ac-lattice diagonal (cyan arrows) below the CO transition at 240 K, referring to the plausible onset of CO stripes [1,2], largely unnoticed in the study before [22].

A close inspection of the ac-modulated superlattices [e.g., those in the red rectangle in Fig. 2(e)] by careful reflection-intensity examinations is shown in Fig. 2(f) and reveals the commensurate [101]/6 [cyan circles, Figs. 2(e) and 2(f)] and vanishing second-harmonics [101]/3 [black arrows, Fig. 2(f)] vectors. In real space, the emergence of a commensurate [101]/6 superlattice directs to an OP of $\sim$31.4 Å in the modulation length. The vanishing second harmonics corresponding to this commensurate superlattice then indeed reflect a unidirectional CO-stripe-modulated essence for the commensurate $\sim$31.4 Å OP, considering high-order harmonics in the conventional CO stripes are customarily damped out by the inherently forbidden fractional super-periodicity [1,18,32,33]. The intensity of the third harmonics {green circles; [101]/2, Figs. 2(e) and 2(f)} nonetheless rises against that of the second
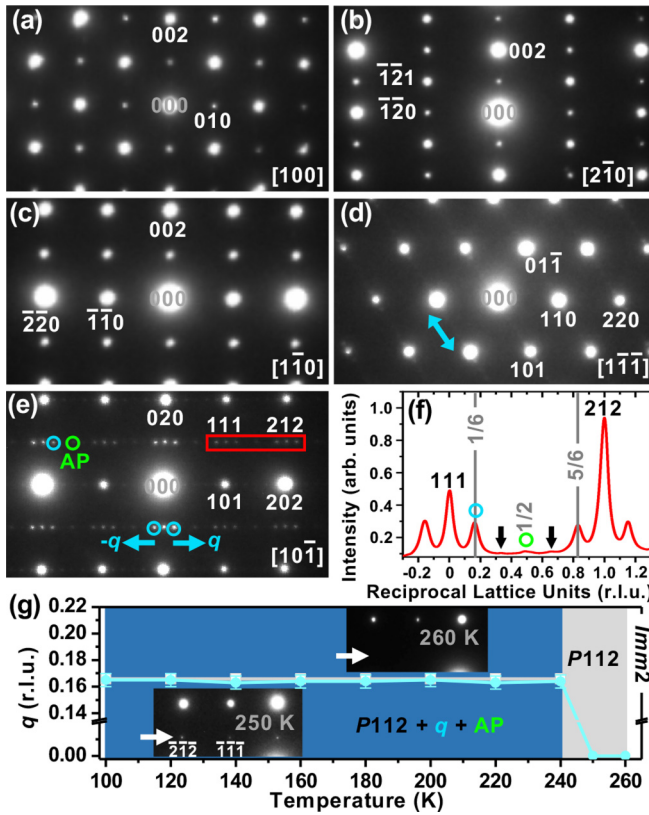
FIG. 2. (a)–(e) Selected-area electron diffraction patterns at 100 K in respective [100], [2–10], [1–10], [1–1-1], and [10–1] zones, with *ac* modulations in (d) and (e) (cyan arrows). (f) Intensity profile of reflections in the red rectangle in (e), unveiling commensurate [101]/6 vector [cyan circle, also in (e)], vanishing second harmonics (black arrows), and antiphase (AP) [101]/2 [green circle, also in (e)]. Commensurate vectors, $\pm q$ in (e). (g) Robust commensurability (cyan; error bars, $\pm3\%$) and AP upon warming up to 240 K. At 240–260 K, commensurate and AP modulations disappear (white arrows, insets) and $P112$ survives. Gray squares, [101]/6 reference.
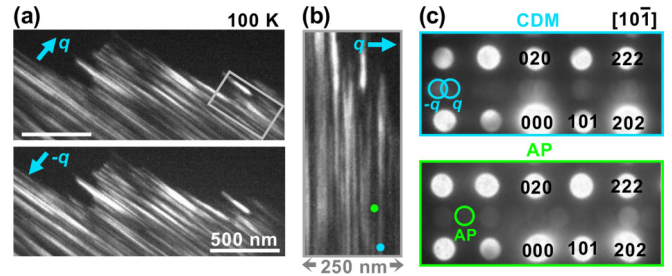

FIG. 3. (a) 100 K dark-field (DF) transmission electron microscopy (TEM) imaging by exploiting $\pm q$ in Fig. 2(e). (b) Blowup of the gray rectangle area in (a). Cyan and green dots, schematic ~5 nm probes impinging the respective bright and dark stripes. (c) The corresponding diffraction to (b), showing commensurate [antiphase (AP)] order of the contributed bright (otherwise dark) stripe. CDM stands for a charge-density modulated order parameter (OP) (see text).

harmonics, suggesting a separate origin from the ~31.4 Å OP and implying an OP otherwise of ~10.5 Å in the modulation length. It is noted that the CMR phases of $(La, Ca)MnO_3$ and $(Pr, Ca)MnO_3$ manganites harbor the conventional CO stripes and an electronically separated metallic phase [17–19]. In the present HMO, the likewise coexistence of two OPs as the manganites mentioned [17–19] could be possible. All these superlattice characteristics in the HMO persist up to 240 K upon warming [Fig. 2(g)], consistent with a reported CO transition at 240 K [22].

Using the commensurate [101]/6 vectors of $\pm q$ [cyan arrows, Fig. 2(e)] for further DF imaging at 100 K, the observed contrast robustness upon $\pm q$ in Fig. 3(a) reveals the characteristic intertwined topology composed by the $\pm q$-contributed bright and otherwise dark stripes at the mesoscopic length scale of 10–40 nm in width and $\geqslant500$ nm in length [see also the blowup in Fig. 3(b)], in distinct difference from the conventional atomically narrow CO stripes at a microscopic length scale [17–19]. Impinging the respective bright and dark stripes with a finite ~5 nm electron probe [cyan and green dots, Fig. 3(b)], the thus-obtained diffraction patterns

in Fig. 3(c) firmly reveal the individual contributions by commensurate ~31.4 Å ([101]/6) and AP ~10.5 Å ([101]/2) OPs.

Using atomic-scale cryogenic STEM at 100 K, we directly image the lattice characteristics of the commensurate OP in Fig. 4(a) (cyan rectangle) and AP OP in Fig. 4(b) (green rectangle). The RT counterpart in Fig. 4(c) shows the A' (superimposed $Hg_{A'}$ and $Mn_{A'}$, thus brighter), A (Mn_A), B' ($Mn_{B'}$), and B (Mn_B) cations schematized in Figs. 4(g) and 4(h) [34]. The LT structural characteristics observed in Figs. 2–4 are firmly reproducible in our repeated LT experiments at 100 K. At RT, all atomic contrasts center on *ac* and *b* axes [Fig. 4(c)]. By contrast, the commensurate [Figs. 4(a) and 4(d)] and AP [Figs. 4(b) and 4(e)] OPs at 100 K display *ac*-modulated Mn_B displacements (guiding colored dots) parallel to the respective vectors of [101]/6 and [101]/2. The *b*-oriented contrast smearing of $Mn_{A'}$ and $Mn_{B'}$ in Figs. 4(a) and 4(b) is associated with the condensation of T_1-phonon modes with characteristic *b*-directed $Mn_{A'}$ and $Mn_{B'}$ displacements in the LT $P112$ symmetry, as depicted in Figs. 4(g) and 4(h) (respective gray and red arrows) [34]. We will come back to this T_1 irreducible representation (IR) in a later group-theoretical discussion.

In the commensurate OP [cyan rectangle, Fig. 4(a)], the Mn_B *ac* displacements display a remarkable cooperative zigzag pattern, with the blue-cyan Mn_B pair at lattice-column marker I being reversed at II and restored at III. Figure 4(d) profiles the displacements of the blue and cyan Mn_B atoms by careful averaging over four respective *ac* rows. Figure 4(f) measures the relative Mn_B displacement $\Delta u(x)$ at each blue-cyan pair of the OP in Fig. 4(d) and unveils a sinusoidallike pattern astonishingly analogous to the theoretical sinusoidal one of charge-density waves [gray line; $\Delta u(x) = \Delta u_0 \cdot \cos(q'x)$, where x is the coordinate, q' is the charge-density-wave wavevector, and Δu_0 is the atomic-displacement maximum at origin] [35]. By contrast, the AP OP [green rectangle, Fig. 4(b); also Fig. 4(e)] exhibits collective off-center *ac* shifts of the olive-green Mn_B pairs. The Fourier transforms of Figs. 4(a) and 4(b) (insets) agree with the respective diffraction patterns in Fig. 3(c), confirming the uniaxial *ac* modulation essence of the commensurate and AP OPs. This modulation characteristic of the OPs is in sharp contrast to the
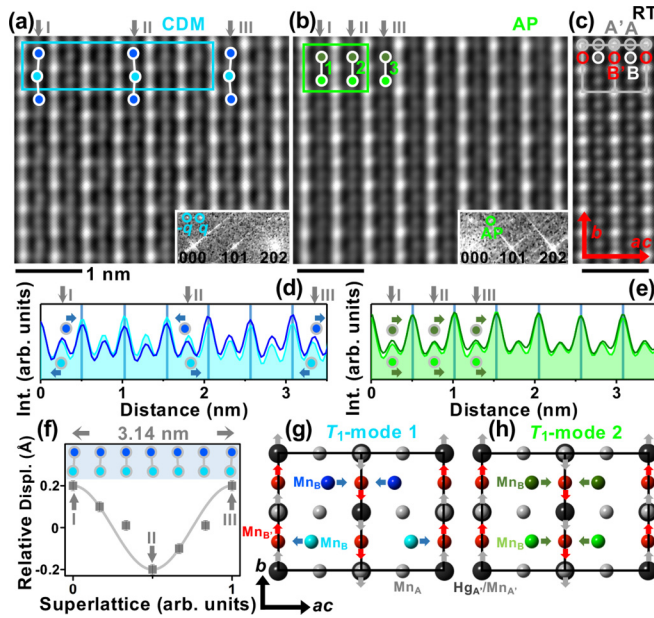
FIG. 4. Bragg-filtered scanning transmission electron microscopy (STEM)- high-angle annular dark-field (HAADF) imaging of (a) charge-density-modulated (CDM) and (b) antiphase (AP) stripes observed in Fig. 3(a) at 100 K. Insets, fast Fourier transforms. Cyan and green rectangles, the order parameters (OPs). Blue-cyan (olive-green) Mn_B pairs, cooperative zigzag (rightward) ac displacements. I, II, and III, lattice-column markers in (d)–(f). 1, 2, and 3, see Fig. 5(c). (c) Bragg-filtered STEM-HAADF imaging at room temperature (RT). Gray cage, primitive lattice. A', A, B', and B, see (g) and (h). (d) Intensity profiles of the respective blue and cyan Mn_B ac rows in the OP in (a), and (e) those of the respective olive and green Mn_B ac rows in (b). Each curve, an average over four ac rows. (f) Relative displacements of the blue-cyan Mn_B pairs (schematic inset) measured in (d), dark gray squares with error bars of ±10%. Gray line, theoretical sinusoidal displacement pattern characteristic of charge-density waves. (g) T_1-phonon mode 1 with inherent zigzag and (h) 2 with face-to-face Mn_B displacements in the primitive $P112$ cell. Arrows, characteristic displacements [34].

FIG. 5. (a) Cryogenic scanning transmission electron microscopy (STEM)- electron energy-loss spectroscopy (EELS) Mn-L probing of $Mn_{A'}$–Mn_A and $Mn_{B'}$–Mn_B rows in charge-density-modulated (CDM) order parameter (OP). Black, blue, and cyan arrows, ac-scanning directions. Blue curve, Mn-L_3 intensity upon blue arrow probing. Gray curve, room temperature (RT) counterpart. (b) Mn-L maps of six blue (top) and cyan (middle) Mn_{B1}–Mn_{B6} and Mn_{A1}–Mn_{A6} (bottom) in (a). Red (blue) arrow, highlighting the spectral redshift (blueshift). (c) Mn-L maps of three olive (top) and green (middle) Mn_{B1}–Mn_{B3} and Mn_{A1}–Mn_{A3} (bottom) in antiphase (AP) OP indicated in Fig. 4(b) (1, 2, and 3). Dashed lines, guides for the eyes.

conventional wisdom of CO stripes that are atomically modulated features perpendicular to the superlattice wavevector [1,2]. In addition, the commensurate and AP OPs surpass the respective primitive T_1-lattice motifs in Figs. 4(g) (blue-cyan Mn_B) and 4(h) (olive-green Mn_B) by the longer-wavelength Mn_B zigzagging and cooperative AP rightward Mn_B displacements [34]. Electronic subtlety in the OPs shall be at play and is tackled in Fig. 5.

In Fig. 5(a), we scrutinize the charge features of the sinusoidallike displaced Mn_B central to the commensurate OP [Figs. 4(a) and 4(f)] using cryogenic STEM-EELS probing for each of the constituent Mn_{B1}–Mn_{B6}. In the presence of persistent liquid-nitrogen bubbling and specimen drift upon the cryogenic STEM-EELS experiment, we optimized the atomic-scale spectral probing by an adequate dwell time of 1 s per pixel (pixel size, 0.5 Å) and an accompanied total acquisition time around 1 min, altogether casting an eligible probing distance of approximately ~3 nm [Fig. 5(a)] that is compatible with the commensurate OP modulation length of ~31.4 Å. Modern state-of-the-art EELS spectrometers with
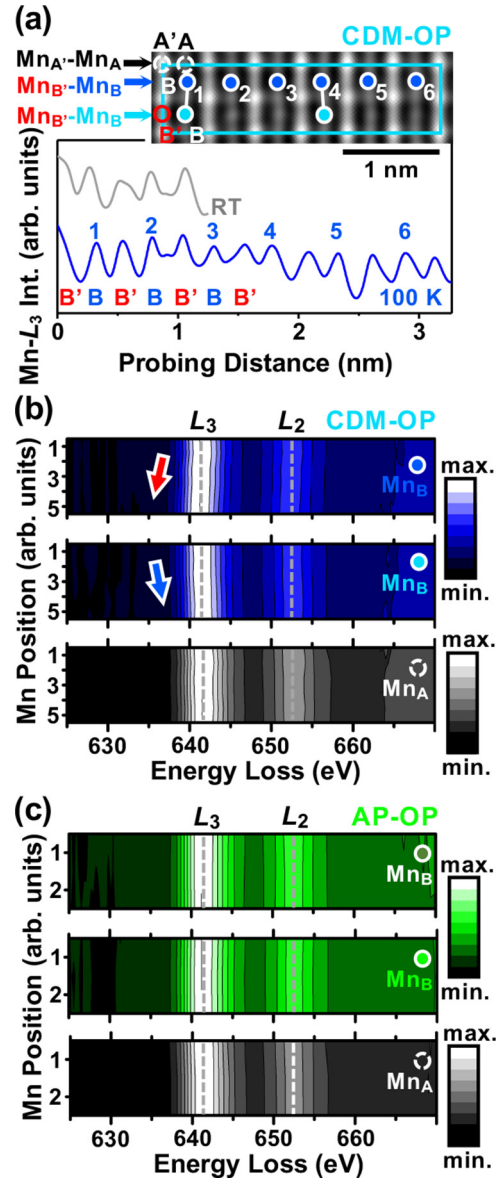
a high-speed detection scheme compared with this rather slow one of ours [27,28] would enable the cryogenic spectral tackling at a longer length scale, potentially addressing the electronic characteristic of Mn_B in the commensurate OP in further details and to be developed in the future.

Upon scanning the electron beam across the row of six blue Mn_B at 100 K in Fig. 5(a), the atomically resolved oscillation
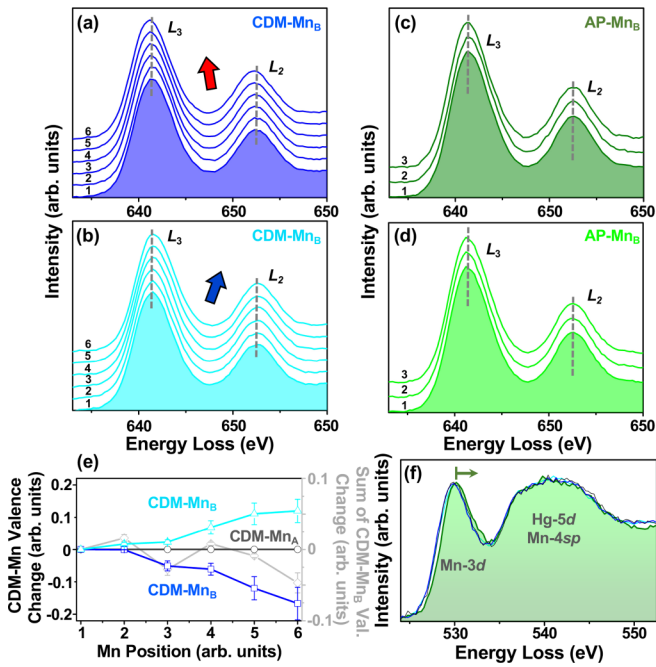
FIG. 6. (a) and (b) The corresponding electron energy-loss spectroscopy (EELS) spectra of respective blue and cyan Mn_{B1}–Mn_{B6} in Fig. 5(b), and Figs. 6(c) and 6(d) being those of respective olive and green Mn_{B1}–Mn_{B3} in Fig. 5(c). Dashed lines, guides for the eyes. Respective red and blue arrows in (a) and (b), highlighting the corresponding spectral red- and blueshift. (e) The readily estimated Mn_B and Mn_A valence changes in charge-density-modulated (CDM) order parameter (OP; left scale) and sum at each blue-cyan Mn_B pair (right scale; gray). Error bars, 10%. (f) The O-K spectra simultaneously acquired at blue and cyan Mn_{B6} and sum of those at Mn_{A1}–Mn_{A6} (thin black). The well-aligned and nearly indistinguishable line shapes of blue, cyan, and thin black spectra of CDM indicate that the related spectral red- and blueshift in (a) and (b), respectively, are firm. Olive and green filled, sum of the O-K spectra at olive and green Mn_{B1}–Mn_{B3} in antiphase (AP) OP. Arrow, $\sim$0.3 eV blueshift.
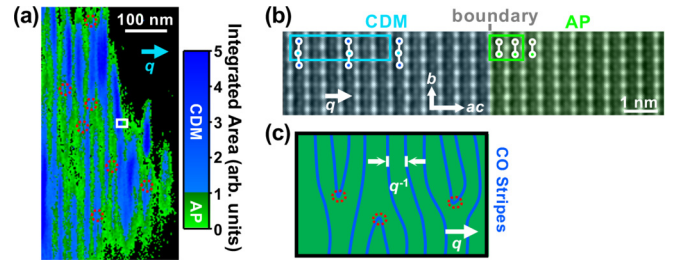

FIG. 7. (a) Mesoscopic charge-density-modulated (CDM; blue) and antiphase (AP; green) stripes, a recasting of Fig. 3(a) in color. (b) Blowup of a CDM-AP boundary schematized as the white box in (a). (c) The conventional atomically narrow charge-ordered (CO) stripes (blue; q, wavevector; q^{-1}, spacing; reproduced from Ref. [21]) embedded in crystalline matrix (green). Dashed-red circles, topological dislocation defects.

of acquired Mn-L_3 spectral intensities (blue; gray, RT counterpart) demonstrates a sensible achievement of atomic-scale cryogenic STEM-EELS. The thus-derived Mn-L maps of blue and cyan Mn_{B1}–Mn_{B6} and Mn_{A1}–Mn_{A6} in the commensurate OP are exhibited in Fig. 5(b). A gradual spectral redshift emerges from the blue Mn_{B1} to Mn_{B6} [red arrow; top panel, Fig. 5(b)] and a gentle blueshift appears from the cyan Mn_{B1} to Mn_{B6} (blue arrow; middle), with the Mn_A being relatively robust (bottom). By contrast, the spectral probing of the AP OP in Fig. 5(c) indicates the absence of likewise spectral shifts in the olive and green Mn_B. The original Mn_B spectra consisting of Fig. 5(b) [Fig. 5(c)] are also displayed in Figs. 6(a) and 6(b) [Figs. 6(c) and 6(d)], revealing that the spectral shifts observed in the commensurate OP [Fig. 5(b)] are indeed robust to both the L_3 and L_2 edges as what a firm Mn L-edge chemical shift should manifest [36].

With the typical chemical redshift of $\sim$1.5 eV for Mn^{3+} compared with Mn^{4+} in ionic limit [36], the maximal redshift (blue) of $\sim$0.25 ($\sim$0.18) eV at the blue (cyan) Mn_{B6} in the commensurate OP in [Figs. 6(a) and 6(b)], determined by the difference in the Gaussian-fitted L_3 peak position with

the Mn_{B1}, would correspond to a valence variation of -0.17 ($+0.12$) from the blue (cyan) Mn_{B1}. The thus-estimated valence changes of each Mn_B and Mn_A in the commensurate OP are shown in Fig. 6(e) (error bars, 10%), with the overall valence change at each blue-cyan Mn_B pair (light gray, right scale) suggesting a charge-modulated Mn_B pattern dissimilar to the theoretical sinusoidal one of charge-density waves [$\rho(x) = \rho_0 \cdot \cos(q'x)$, where ρ_0 is the charge-variation maximum at origin] [35]. The sinusoidallike atomic modulation in Fig. 4(f) of the commensurate OP is accompanied with an intricate nonsinusoidallike charge counterpart [Fig. 6(e)], indicating a CDM OP [8] by borrowing the sinusoidal analogy of charge-density waves in theory [35]. Future cryogenic STEM-EELS studies by the state-of-the-art high-speed EELS facility [27,28] shall be able to further address this subtle charge modulation of the CDM OP. Although the AP OP is immune from such charge variations [Figs. 5(c) and 6(c) and 6(d)], the Mn-3d component of the O-K spectrum is blueshifted by $\sim$0.3 eV compared with that of the CDM [olive arrow, Fig. 6(f)]. This feature refers to a further gapping in the O-2p and Mn-3d hybridization by $\sim$0.3 eV for the AP OP (i.e., a more insulating OP than the CDM).

With the cryogenic structural (Fig. 4) and spectral investigations (Figs. 5 and 6), the CO transition at 240 K of the HMO is visibly irrelevant with the conventional CO stripes [1,2] and rather arises from the emergence of CDM and AP OPs, which are largely undocumented forms of COs in correlated electron systems [1–3]. As indicated in Fig. 7(a) [a recasting of Fig. 3(a) in color], the two OPs constitute a mesoscopic topology of intertwining stripes (blue, CDM domains; green, AP ones). An enlarged view of the CDM-AP boundary shows atomically sharp characteristics without noticeable structural distortions [Fig. 7(b)], lifting the possibility of the observed topology [Fig. 7(a)] as a strain-driven pattern formation [37]. Intriguingly, the mesoscopic texture in Fig. 7(a) qualitatively mimics the microscopic topology of conventional CO stripes in Fig. 7(c) (reproduced from Ref. [21]), where the periodic stripes are characteristically perpendicular to the modulated vector q [1,2,20,21], and features similar to the ubiquitous topological dislocation defects in Fig. 7(c) (dashed red circles) are also found in Fig. 7(a).

Considering the overall charge neutrality maintained in the conventional CO-stripe texture in Fig. 7(c) [1,2,20,21], the comparability of the striped AP/CDM area ratio of $\sim \frac{1}{4}$ in Fig. 7(a) with the nominal quarter hole doping by Hg^{2+} could be enlightening. Supposedly, the AP OP could be relatively positive due to the further gapping of ~ 0.3 eV in Fig. 6(f) and may readily accommodate the doped hole thereby. Meanwhile, the CDM OP would be electrostatically negative, as suggested by the negative net charge in Fig. 6(e). The mesoscopic striped topology with the quarter AP-CDM area ratio in Fig. 7(a) could then correspond to an electrostatic-neutral landscape like the conventional CO stripes in Fig. 7(c) [1,2,20,21] and delineates the unique electronic contour of the HMO. While the mesoscopic texturing in the HMO could be of such an electrostatic origin, further theoretical tackling of the fundamental Coulomb characteristics of the exotic CDM and AP OPs would be essential for underlining the grand physics and is a separate work on its own. Our cryogenic STEM-EELS unraveling of this distinct CO phenomena is, in effect, assisted by an unambiguity in the CO modulated vectors [Figs. 2(d) and 2(e)]. The firm pinpointing of the *ac* modulations is based on an effective group-theoretical practice for OPs [34], instead of the routine exploitation of exhausted searches in real and reciprocal spaces [4–19].

According to the Landau theory of phase transitions, symmetry breaking is linked to the condensed phonon instability in the Brillouin zone, and a group-theoretical analysis of the characteristic IR can reveal the OP-symmetry direction and domain topology [25,34,38]. Taking ferroelectric $BaTiO_3$ classics for example, the symmetry breaking from high-temperature (HT) $Pm\bar{3}m$ to RT $P4mm$ corresponds to a condensed zone-center instability at IR Γ_4^- with a uniaxial $(0, 0, a)$-OP symmetry and six degenerate domains, in agreement with the *c*-oriented polarization and the intrinsic topology of abundant domains [39,40].

Accordingly, we have proceeded to analyze the symmetry breaking from RT $Imm2$ (Fig. 1) to LT $P112$ (Fig. 2) in HMO and derived the IR-T_1 lattice instability in Fig. 1(a), with an (a, c)-oriented OP direction and a two-component OP space with degenerate domains [34,40]. Indeed, the *ac* modulations [Figs. 2(d) and 2(e)], pertinent CDM and AP OPs (Figs. 3–6), and concomitant topology [Fig. 7(a)] in coherence with the two-component OP space are all experimentally resolved. The charge-lattice entanglements in the CDM and AP OPs not only dictate a symmetry breaking but are apparently compatible with the Landau group-theoretical practice for OPs [34]. This latter notion is further examined using the intricate 45° difference in the conventional

CO stripes in respective La_2CuO_4-family cuprates [5] and isostructural nickelates [11–16], considering the CO stripes also exhibit a significant charge-lattice coupling [1,2,41]. Although the LT symmetries remain inconclusive, a group-theoretical analysis on provisory LT $P4_2/ncm$ (*Bmab*) in the cuprates [32] (nickelates [42]) from HT $I4/mmm$ indicates the $(a,0)$-OP symmetry upon IR X_3^+ [(a, a) upon IR X_2^+] with a two-component OP space [34]. This 45° angle between $(a,0)$ and (a, a) coincides with the aforementioned 45° angular difference, and the characteristic OP space corresponds to Fig. 7(c) [21]. The conventional CO stripes in the CMR $(La,Ca)MnO_3$ and $(Pr,Ca)MnO_3$ manganites [17–19] were more recently revised to be charge-density-wavelike with a fractional Mn charge disproportionation like that of the CDM hereby [Fig. 6(e)] [43–45], stimulating future cryogenic STEM-EELS and group-theoretical undertaking with the state-of-the-art EELS apparatus with high-speed detections [27,28].

IV. CONCLUSIONS

Electronic orders and topology stand at the core of solid-state physics and continuously push the limit of experimental probing techniques [46]. Direct observations of the OPs and intertwined topology, which have been long awaited, shall lead to enlightening aspects on the physics. Our cryogenic STEM-EELS study in a correlated manganite insulator represents a preliminary step along this line and prompts for extensive atomic-scale explorations of a plethora of commensurate and incommensurate COs in matters at LT [4–19,35,41,43–47], where the interplay of OPs and complex topology remain largely unsettled territories, and our group-theoretical scrutiny on broken symmetries in electronic phase transitions might facilitate associated understanding.

[1] E. Fradkin, *Modern Theories of Many-Particle Systems in Condensed Matter Physics*, edited by D. C. Cabra (Springer-Verlag, Berlin, Heidelberg, 2012), Chap. 2.

[2] S. A. Kivelson, I. P. Bindloss, E. Fradkin, V. Oganesyan, J. M. Tranquada, A. Kapitulnik, and C. Howald, Rev. Mod. Phys. **75**, 1201 (2003).

[3] M. Imada, A. Fujimori, and Y. Tokura, Rev. Mod. Phys. **70**, 1039 (1998).

[4] S.-W. Cheong, G. Aeppli, T. E. Mason, H. Mook, S. M. Hayden, P. C. Canfield, Z. Fisk, K. N. Clausen, and J. L. Martinez, Phys. Rev. Lett. **67**, 1791 (1991).

[5] J. M. Tranquada, B. J. Sternlieb, J. D. Axe, Y. Nakamura, and S. Uchida, Nature **375**, 561 (1995).

[6] T. Wu, H. Mayaffre, S. Krämer, M. Horvatić, C. Berthier, W. N. Hardy, R. Liang, D. A. Bonn, and M.-H. Julien, Nature **477**, 191 (2011).

[7] S. Gerber *et al.*, Science **350**, 949 (2015).

[8] R. Arpaia, S. Caprara, R. Fumagalli, G. De Vecchi, Y. Y. Peng, E. Andersson, D. Betto, G. M. De Luca, N. B. Brookes, F. Lombardi, M. Salluzzo, L. Braicovich, C. Di Castro, M. Grilli, and G. Ghiringhelli, Science **365**, 906 (2019).

[9] M. J. Lawler, K. Fujita, J. Lee, A. R. Schmidt, Y. Kohsaka, C. K. Kim, H. Eisaki, S. Uchida, J. C. Davis, J. P. Sethna, and E.-A. Kim, Nature **466**, 347 (2010).

[10] A. Mesaros, K. Fujita, H. Eisaki, S. Uchida, J. C. Davis, S. Sachdev, J. Zaanen, M. J. Lawler, and E.-A. Kim, Science **333**, 426 (2011).

[11] S. M. Hayden, G. H. Lander, J. Zarestky, P. J. Brown, C. Stassis, P. Metcalf, and J. M. Honig, Phys. Rev. Lett. **68**, 1061 (1992).

[12] C. H. Chen, S.-W. Cheong, and A. S. Cooper, Phys. Rev. Lett. **71**, 2461 (1993).

[13] J. M. Tranquada, D. J. Buttrey, V. Sachan, and J. E. Lorenzo, Phys. Rev. Lett. **73**, 1003 (1994).

[14] S.-H. Lee and S.-W. Cheong, Phys. Rev. Lett. **79**, 2514 (1997).

[15] J. M. Tranquada, K. Nakajima, M. Braden, L. Pintschovius, and R. J. McQueeney, Phys. Rev. Lett. **88**, 075505 (2002).

[16] R. Kajimoto, K. Ishizaka, H. Yoshizawa, and Y. Tokura, Phys. Rev. B **67**, 014511 (2003).

[17] S. Mori, C. H. Chen, and S.-W. Cheong, Nature **392**, 473 (1998).

[18] C. H. Chen, S.-W. Cheong, and H. Y. Hwang, J. Appl. Phys. **81**, 4326 (1997).

[19] C. H. Chen, S. Mori, and S.-W. Cheong, Phys. Rev. Lett. **83**, 4792 (1999).

[20] S. A. Kivelson, E. Fradkin, and V. J. Emery, Nature **393**, 550 (1998).

[21] K. Sun, B. M. Fregoso, M. J. Lawler, and E. Fradkin, Phys. Rev. B **78**, 085124 (2008).

[22] W.-T. Chen, C.-W. Wang. H.-C. Wu, F.-C. Chou, H.-D. Yang, A. Simonov, and M. S. Senn, Phys. Rev. B **97**, 144102 (2018).

[23] P.-W. Lee, M. H. Lee, S.-C. Lee, C.-P. Chang, Y.-C. Lai, G. Y. Guo, Y.-H. Chu, W.-L. Lee, C. H. Chen, and M.-W. Chu, JEOL News **52**, 11 (2017).

[24] P. W. Lee, V. N. Singh, G. Y. Guo, H.-J. Liu, J.-C. Lin, Y.-H. Chu, C. H. Chen, and M.-W. Chu, Nat. Commun. **7**, 12773 (2016).

[25] M. H. Lee, C.-P. Chang, F.-T. Huang, G. Y. Guo, B. Gao, C. H. Chen, S.-W. Cheong, and M.-W. Chu, Phys. Rev. Lett. **119**, 157601 (2017).

[26] I. E. Baggari, B. H. Savitzky, A. S. Admasu, J. Kim, S.-W. Cheong, R. Hovden, and L. F. Kourkoutis, Proc. Natl. Acad. Sci. **115**, 1445 (2018).

[27] D. J. Baek, M. J. Zachman, B. H. Goodge, D. Lu, Y. Hikita, H. Y. Hwang, and L. F. Kourkoutis, Microsc. Microanal. **24**, 454 (2018).

[28] W. Zhao, M. Li, C.-Z. Chang, J. Jiang, L. Wu, C. Liu, J. S. Moodera, Y. Zhu, and M. H. W. Chan, Sci. Adv. **4**, eaao2682 (2018).

[29] R. Hovden, A. W. Tsen, P. Liu, B. H. Savitzky, I. E. Baggari, Y. Liu, W. Lu, Y. Sun, P. Kim, A. N. Pasupathy, and L. F. Kourkoutis, Proc. Natl. Acad. Sci. **113**, 11420 (2016).

[30] D. B. Williams and C. B Carter, *Transmission electron microscopy* (Plenum Press, New York, 1996).

[31] See Supplemental Material at http://link.aps.org/supplemental/10.1103/PhysRevB.103.115130 for additional information on the RT structure, domain evolutions, and otherwise experimental details.

[32] J. M. Tranquada, J. E. Lorenzo, D. J. Buttrey, and V. Sachan, Phys. Rev. B **52**, 3581 (1995).

[33] J. M. Tranquada, J. D. Axe, N. Ichikawa, Y. Nakamura, S. Uchida, and B. Nachumi, Phys. Rev. B **54**, 7489 (1996).

[34] H. T. Stokes and D. M. Hatch, *Isotropy subgroups of the 230 crystallographic space groups* (World Scientific Publishing, Singapore, 1988); *ISOTROPY Software* (Department of Physics and Astronomy, Brigham Young University, Provo; http://stokes.byu.edu/isotropy.html). The symmetry breaking in the HMO from *Imm*2 to *P*112 is subject to degenerate IR T_1 and IR T_2, which only differ in the choice of crystallographic origins. For convenience, we choose IR T_1 with the origin at $(0,0,0)$.

[35] G. Grüner, *Density waves in solids* (Perseus Publishing, Cambridge, 1994).

[36] C.-P. Chang, M.-W. Chu, H. T. Jeng, S.-L. Cheng, J. G. Lin, J.-R. Yang, and C. H. Chen, Nat. Commun. **5**, 3522 (2014).

[37] A. K. Tagantsev, L. E. Cross, and J. Fousek, *Domains in Ferroic Crystals and Thin Films* (Springer, New York, 2010).

[38] J. C. Tolédano and P. Tolédano, *The Landau Theory of Phase Transitions* (World Scientific Publishing, Singapore, 1987).

[39] D. M. Hatch and H. T. Stokes, Phys. Rev. B **65**, 014113 (2001).

[40] Six symmetry-degenerate domains in *P*4*mm* and *Imm*2: $(0, 0, a) = (a, 0, 0) = (0, a, 0) = (0, 0, -a) = (-a, 0, 0) = (0, -a, 0)$. Eight symmetry-degenerate domains in *P*112 of the HMO, $(a, c) = (c, a) = (-a, c) = (-c, a) = (a, -c) = (c, -a) = (-a, -c) = (-c, -a)$, are reduced to two, $(a, c) = (-a, -c)$, by the nonorthogonal γ.

[41] X. Zhu, Y. Cao, J. Zhang, E. W. Plummer, and J. Guo, Proc. Natl. Acad. Sci. **112**, 2367 (2015).

[42] G. H. Lander, P. J. Brown, J. Spalek, and J. M. Honig, Phys. Rev. B **40**, 4463 (1989).

[43] G. C. Milward, M. J. Calderón, and P. B. Littlewood, Nature **433**, 607 (2005).

[44] J. C. Loudon, S. Cox, A. J. Williams, J. P. Attfield, P. B. Littlewood, P. A. Midgley, and N. D. Mathur, Phys. Rev. Lett. **94**, 097202 (2005).

[45] L. Brey, Phys. Rev. Lett. **92**, 127202 (2004).

[46] N. D. Mermin, Rev. Mod. Phys. **51**, 591 (1979).

[47] Y.-D. Chuang, A. D. Gromko, D. S. Dessau, T. Kimura, and Y. Tokura, Science **292**, 1509 (2001).